Advanced Materials Technologies

ADVANCED MATERIALS TECHNOLOGIES
www.advmattechnol.com

RESEARCH ARTICLE OPEN ACCESS

Ultra-Thin Soft Pneumatic Actuation for Minimally Invasive Neural Interfacing

Lawrence Coles[1,2] | Joe G. Troughton[1,2] | Alejandro Carnicer-Lombarte[1] | George G. Malliaras[1] | Christopher M. Proctor[1,2]

[1]Department of Engineering, University of Cambridge, Cambridge, UK | [2]Institute of Biomedical Engineering, Engineering Science Department, University of Oxford, Oxford, UK

Correspondence: Christopher M. Proctor (christopher.proctor@eng.ox.ac.uk)

Received: 16 October 2025 | **Revised:** 12 December 2025 | **Accepted:** 15 December 2025

Keywords: bioelectronics | neural interface | shape actuation | soft-robotics

ABSTRACT

Soft-robotic fluidic actuation allows dynamic control of the shape and position of ultra-flexible bioelectronic implants inside the body. While several actuation approaches have been proposed, all face significant limitations preventing clinical translation. Here, the use of laser-based fabrication techniques for selective welding of Parylene C to create fluidic actuation chambers capable of withstanding high pressures over repeated actuations is explored. The ultra-thin Parylene C fluidic chamber design with an electrode array for peripheral nerve interfacing is integrated, serving as a proof-of-concept for Parylene C-only fluidic actuation. Through thermoforming, it is molds Parylene C into a cuff which straightens and stiffens under fluidic pressure to aid implantation, before wrapping around the nerve bundle during depressurization. This is demonstrated on the sciatic nerve of a rodent model, achieving good electrophysiological recording resolution due to the conformal wrapping of the cuff. With the development of ultra-thin Parylene C based fluidic systems, it is aimed to push the boundaries of bioelectronic systems, offering new possibilities for monolithically integrated, minimally invasive interfacing.

1 | Introduction

Periphery nerve interfaces (PNI) provide direct access to nerve fibers, granting higher spatial and temporal selectivity than traditional non-invasive approaches, facilitating precise recording and modulation of nerve activity [1]. PNIs represent a rapidly evolving field of implantable devices, offering new potential bioelectronic-based treatments. PNIs are being increasingly adopted to address myriad conditions, including neuropathic chronic pain, metabolic conditions, and epilepsy. Notably, vagus nerve stimulation has already gained approval for treating depression [2] and epilepsy [3], and sacral nerve stimulation for overactive bladder control [4–6]. Additionally, PNIs are being adapted for use in brain-computer interfaces, providing a platform for the control of prosthetic limbs [7–9]. PNIs typically target larger nerve bundles to enable the use of simpler fabrication strategies to achieve chronically stable implantable devices, and reduce implantation complexity. Penetrating intra-neural devices offer the highest selectivity by allowing the electrodes to directly interface with the individual fascicles, however, the invasiveness can trigger a large foreign body response within the nerve, limiting chronic stability [10–12]. Alternatively, extra-neural electrodes, which encase the nerve, usually in the form of a cuff, offer reduced surgical trauma, eliciting a smaller foreign body reaction and requiring an easier surgical procedure, are often favored for long-term use, albeit with reduced spatial selectivity. Peripheral nerve interfacing is

Lawrence Coles and Joe G. Troughton contributed equally to this work.

This is an open access article under the terms of the Creative Commons Attribution License, which permits use, distribution and reproduction in any medium, provided the original work is properly cited.

© 2025 The Author(s). *Advanced Materials Technologies* published by Wiley-VCH GmbH

also a regular part of clinical practice during neural procedures, including neurotomy and neurolysis [13–15]. Here, continuous measurement of nerve function would be of great value, but is currently limited to sporadic measurement using handheld metallic probes [16, 17].

There is growing demand for soft, flexible materials in the production of peripheral nerve interfaces, as this helps to minimize foreign body reactions to chronically implanted devices [11, 18, 19], and allows for continuous monitoring of interoperative nerve function without risking mechanical damage to the nerves. Research into biocompatible and chemically inert materials such as polyimide and Parylene C is gaining momentum, particularly for crafting pre-formed cuffs [12], to create thin-film devices that can wrap safely around small nerve bundles.

Despite recent progress in the development of flexible and stretchable thin-film nerve cuffs that mitigate some challenges associated with current devices, there remains a need for novel minimally invasive implantation techniques. Such innovations are crucial for diminishing surgical invasiveness, thereby enhancing the accessibility of peripheral nerve devices. The incorporation of soft robotics into nerve interfaces, propelled by breakthroughs in soft material science and advanced fabrication methods, presents promising avenues for achieving less invasive implantation strategies [20–23]. This integration aims to streamline the surgical process, potentially transforming patient experiences by offering safer and more efficient device implantation options.

There has been considerable recent work looking at strategies to enable some level of autonomous device wrapping to reduce surgical complexity during the implantation of these PNIs. Approaches such as using shape memory materials [20, 24] and materials that respond to body temperature or the local aqueous environment [25, 26] have been investigated. Yet they lack the ability to reverse that initial shape change within the body, reducing surgical translatability due to the need for real-time adjustment. Recently, reversible actuation has been demonstrated based on electrochemical actuation [23], though this requires exotic materials not necessarily suitable for clinical translation. Furthermore, many of these approaches suffer from relatively slow actuation speeds, in the range of seconds to minutes, reducing their attractiveness for interoperative care. Table 1 gives an overview of these published works, while a more comprehensive overview of actuating devices for biomedical applications can be found in the excellent recent review from Dong and Malliaras [27]. Fluidic-based soft robotics can provide a potential solution, where the shape actuation can be reversibly controlled in real time with pressure-driven fluidic delivery within the implant [21, 22, 28, 29].

In this work, we investigate the fabrication of a Parylene C fluidic chamber, based on laser cutting and welding [33], and combine it with thin-film electronics to create a peripheral nerve cuff. By optimizing laser parameters, we demonstrate the simultaneous cutting and welding of two Parylene C layers to form a hermetically sealed fluidic chamber capable of holding sufficient pressure to enable device actuation. This laser formed fluidic chamber is further treated with thermoforming techniques to develop a self-wrapping cuff for peripheral nerve interfacing that can be actuated multiple times with minimal degradation of mechanical or electrical performance. The actuation of this device is performed using pneumatic expansion, to stiffen and straighten the devices for implantation and positioning. The simplicity and speed of actuation of these devices represent a step-change in the realm of actuated PNI devices, requiring nothing more than fluidic pressure to place and reposition the device multiple times at speed. Our work demonstrates the potential of this thin-film soft robotic approach to creating ultra-thin, shape-changing implants, envisaging their future application in interoperative care, and lays the groundwork for future innovations in thin-film shape-changing bioelectronic devices that provide minimally invasive implantation approaches.

2 | Results

2.1 | Development of Laser Welded Parylene C Fluidic Chambers

The initial focus of this work was the use of laser-based processing of Parylene C to create fully sealed fluidic chambers that enables shape-changing of thin-film neural interfaces via fluidic actuation. The concept of using laser-based processing to form soft-robotic devices has been shown previously with thermoplastic polyurethane to create devices that can be implanted into the heart via a catheter [34]. However, previous approaches have used relatively thick polymer sheets (>50 μm), reducing the conformability and flexibility of finished devices. On the other hand, Parylene C, has been regularly used in the fabrication of fully conformable and flexible thin-film (<20 μm) neural interfaces [35–38], but presents significant challenges in creating spatially defined bonds between layers due to its highly chemical inert nature. By applying laser-induced bonding to Parylene C, we aimed to create fluidic actuators that retain the flexibility and conformability of the thin-film Parylene C substrate in a simple, direct-write approach. By combining this thin, flexible, laser-bonded Parylene C fluidic component with well-established thin-film electronics comprising layers of Parylene C, Au, and poly(3,4-ethylenedioxythiophene) polystyrene sulfonate (PEDOT:PSS), we created a neural interface device that could be repeatedly actuated to enable minimally invasive implantation and repositioning.

It is well known that Parylene C can be selectively milled and shaped through laser machining [39–44]. When this is done with a long-wavelength laser, such as a 10.6 μm CO_2 laser, the dominant interaction mechanism is phonon absorption which causes rapid, localized heating of the material, eventually leading to thermal breakdown, manifest as cutting, along with a heat-affected zone (HAZ). By sequentially depositing two thin layers of Parylene C, separated with an anti-adhesive soap layer, and treating with such a laser, we found that this HAZ includes a region in which the two layers of Parylene C fuse into a homogenous material along the edge of the laser cut (Figure 1A i–iii). Further, we found that, by reducing the laser power, we were able to induce this HAZ, including the local fusing of the two layers, without causing full ablation of the material (hear-after simply referred to as welding, Figure 1A iv). These processes are combined to create a sealed fluidic chamber, with locally welded areas independent of the chamber outline.

TABLE 1 | Comparison of key parameters of published self-actuating nerve cuffs.

Ref.	Actuation Mechanism	Device Thickness	Response Time	Reversable	Biocompatible	Requires Continuous Input
[30]	Shape Memory Polymer Softening	30 μm	20 min	No	Yes[1]	No
[20]	Shape Memory Polymer Softening	102 μm	10 s	No	Yes[2]	No
[26]	Hydrogel Swelling	70–135 μm	30 s	No	Yes[1]	No
[17]	Dissolvable Layer	100 μm	15 s	No	Yes[2]	No
[23]	Electrochemical	9 μm	2 s	Yes	Unknown[3]	Yes (electrical)
[31]	Water Triggered Contraction	150 μm	10 min	No	Yes[2]	No
[29]	Fluidic	305 μm 2.28 mm in use	45 s	Yes	Yes[2]	Yes (fluidic) or fill with PDMS
[32]	Dissolvable Layer	1 μm	10 s	No	Unknown[3]	No
This Work	Pneumatic	12 μm	5 s	Yes	Yes[2]	No

[1)]Biocompatibility assessed in the publication

[2)]Biocompatibility assumed from use of standard biocompatible materials

[3)]Biocompatibility unclear due to use of non-standard materials and with no testing done

To investigate the integrity of the bonding between Parylene C layers from both the cutting and the welding processes, we first looked at tensile testing using a motorized force measuring system. This was used to examine the maximal force that a bonded sample could hold before breaking. We found that, when using the laser to cut the Parylene C layers, there was a significant increase in the resulting bond strength above 3.3 W power (Figure 1B), indicating the power delivery into the cutting sites was enough to form HAZs that effectively welded the two Parylene C layers. At powers above 4.5 W, the bond strength plateaued at a maximum bond tensile-breaking strength of 19.6 ± 0.6 MPa. In practice, when increasing the power beyond 4.5 W, while the resulting bond formation did not increase in strength, the width of the cut through the Parylene C increased as more of the material was ablated. For the formation of fluidic chambers for implantable devices, using the lowest power needed for maximal bond strength potentially allows for creation of smaller designs, enabling devices capable of interfacing with harder-to-reach clinical targets.

A welded bond with slightly higher strength is formed when the two layers are welded using a reduced laser power of 0.24 W (Figure 1B) to form a bond with a tensile breaking strength of 20.5 ± 0.8 MPa, without cutting the two layers. A reduction in bond strength when the power is increased past 0.24 W laser power indicates that the additional power starts to ablate the top layer of Parylene C, consequently compromising the integrity of the welded area, and therefore the resulting bond strength. The significant reduction in strength between the 0.45 W tested for laser welding and the 0.6 W tested for laser cutting is caused by the laser starting to cut fully through the Parylene C layers without the formation of significant HAZs. With both cutting and welding producing bonds with similar tensile breaking strengths, it can be concluded that either approach could be used to create the desired fluidic chamber.

When attempting to outline a full fluidic chamber, a hermetic seal in the Parylene C layers is essential to enable pneumatic actuation, with any breaks in the welding sites leading to leaks in the fluidic chamber during pressurization, preventing actuation. One method to ensure there are no leaks, thereby guaranteeing the integrity of the fluidic chamber, is to combine a "cutting pass" and a "welding pass" in the outline of the device. This way, any defects in the Parylene C welding during one pass, are covered by the other. For this, the spacing between the cutting and welding passes was examined to identify the optimal distance between them when producing the outline of the fluidic chamber to create a combined welded bond. It is worth noting that we limit this investigation to two passes: one cutting and one welding. While it is may be of some benefit to add additional welding passes, these rapidly increase the overall footprint of the device, negating the advantages of this "minimally invasive" approach. It could, however, be of great interest to introduce internal "tie" points within the fluidic chamber, to minimize vertical expansion in sensitive tissues, and this is an area that will be explored inf future works.

When identifying the optimal offset between the two processed areas, the laser cutting power was set at 4.5 W and the welding power set at 0.24 W, as the two previously identified optimums. By using the lowest suitable laser cutting power, the width of the resulting ablation line after cutting was minimized, enabling a smaller offset between the cutting and welding site, reducing the overall welding footprint, and thereby allowing the formation of smaller fluidic chambers. Tensile testing was again performed on straight bond-line samples following the same methodology as used for Figure 1B. After tensile testing, an offset of 0.3 mm between the cutting and welding sites resulted in the strongest overall bond, with a resulting bond-breaking strength of 24.2 ± 0.6 MPa (Figure S1). This can be compared to the ultimate tensile strength of pristine Parylene C, measured in the same geometry

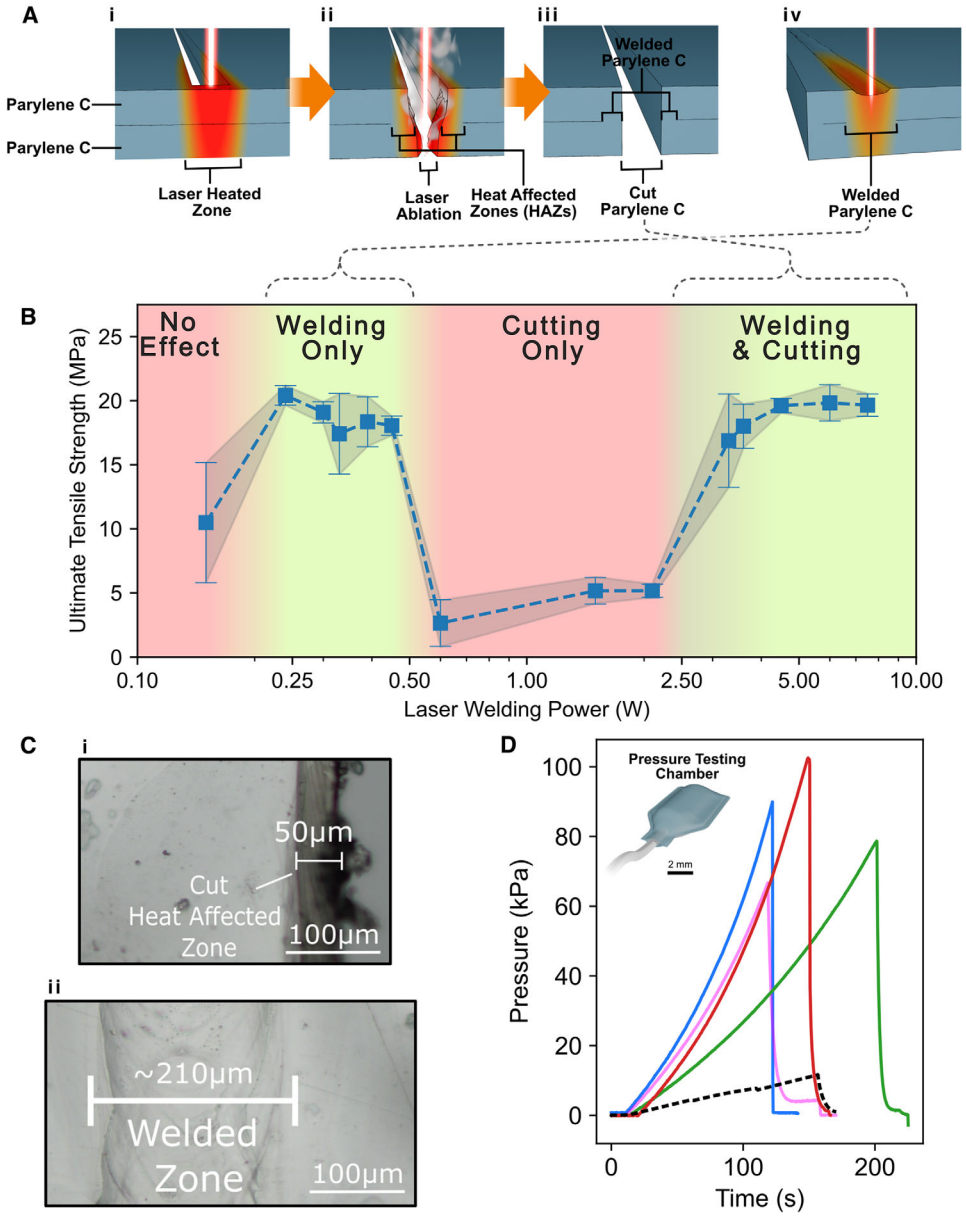

FIGURE 1 | Characterization and formation of the laser welding. (A) Overview of the cutting and welding process used to form Parylene C fluidic chamber. (i) Cutting through the two layers of Parylene C, causing the creation of a laser-heated zone. (ii) Full laser ablation of the two Parylene C layers creating both the outline of the device and Heat Affected Zones on either side of the cutting site. (iii) After cutting, the Parylene C in the Heat Affected Zones is welded together, forming the fluidic chamber. (iv) By reducing the laser power, welding can be achieved between the Parylene C layers without cutting through the two layers. (B) Tensile strength of the bonded Parylene C layers when treating with the laser at increasing powers. Data are presented as average tensile strengths ± standard deviation over 3 independently fabricated samples. (C) Optical images showing the resultant Parylene C bonded areas after laser processing. (i) The Heat Affected Zone as a result of cutting through the two Parylene C layers. (ii) The resultant welding of the two Parylene C layers created through the reduction in laser power. (D) Plots of the pressure in fluidic chambers fabricated with both cutting and welding lines with a 0.3 mm separation, while being inflated with air at 1 ml/min until device failure. Solid colored lines represent devices from this work, while the dash black line shows data adapted from a previous report on silicon-base fluidic devices [21]. Inset is a representation of the chamber design used for this pressure testing.

using a single piece of 4 μm Parylene C folded and cut to resemble the bond breaking samples (inset of Figure S1), which was found to be 73.7 ± 2.2 MPa (data not shown).

An alternative approach to increase the bond strength may be direct engineering of the HAZ extents. In our investigations we found that there was little variation in the optically observable extents of the HAZ with varying laser power. However, in the welding & cutting regime it was found that, as power increased, so the width of the cut (the kerf width) increased, but the extent of the HAZ beyond the cut region remained constant. A route to directly controlling this width would be expanding the laser spot by defocusing the laser. While this was not explored here, it remains an approach that should be explored in future works.

Whilst the use of the combination of cutting and welding did not result in an overall stronger bond between the two Parylene C layers, in practice when creating full fluidic chambers it enabled proper welding along the fluidic chamber circumference by covering inconsistencies in laser power delivery with the two welding passes to create fully sealed chambers. Therefore, employing both cutting and welding, with an offset between, allowed for the compensation of minor inconsistencies in the HAZs that might occur in either the cutting or welding regions due to inconsistent power delivery.

It is worth noting that the optimization process carried out here was performed with the laser focused at the surface of the upper Parylene C layer, 50.8 mm from the primary focusing lens. At focus, the beam width used was ~180 μm, consistent with the width of the welding zone observed (Figure 1Cii). For this system the depth of focus (defined as the length over which the beam diameter varies by less than 10%) can be calculated to be approximately ±1.4 mm from the focal point, meaning the power variation due to defocus throughout the Parylene C stack (8 μm total) is negligible. If, however, a wider welding area was desired, this could be easily achieved by focusing the laser above or below the sample and adjusting the power used accordingly. If, for example, a welding zone of around 400 μm was desired, rather than ~210 μm, the beam could be defocused by around 2.4 mm to double the spot size at the sample. This would increase the spot area by a factor of 4, meaning the power would also have to be increased by a factor of 4 to achieve the same welding strength, in this case increasing the power to 0.96 W.

After identifying the optimal laser welding settings to form a sealed fluidic chamber, the maximum pressure a thin-film Parylene C fluidic chamber could withstand was investigated. Using the identified laser power parameters of 4.5 W cutting power and 0.24 W welding power with a 0.3 mm offset, a 5 × 10 mm rectangular fluidic chamber was laser cut from two 4 μm layers of Parylene C separated by an anti-adhesive soap layer. When inflated using air, we found that the devices were able to hold 78 ± 12 kPa of pneumatic pressure (Figure 1D).

2.2 | Development of an Actuated Peripheral Nerve Cuff

To evaluate the concept of integrating a Parylene C based soft fluidic chamber with thin-film electronics for minimally invasive nerve interfacing, we created a peripheral nerve cuff stimulator. We integrated the Parylene C ultra-thin actuator, made from two laser-bonded 4 μm Parylene C layers as described above, with thin-film electronics to create a thin-film actuatable bioelectronic nerve cuff that can record from peripheral nerves after using fluidic actuation for implantation (Figure 2A,B; Figure S2). Thin-film electronics were created on a Parylene C substrate using photolithography to pattern Au and PEDOT:PSS electrodes and consisted of two sets of four 0.4 μm diameter circular electrodes designed to be positioned radially around the nerve, and a set of four 0.45 × 3.45 mm rectangular electrodes located between the two sets of circular electrodes forming circumferential ring-type electrodes. These were subsequently attached to the Parylene C fluidic actuator to yield a total device thickness of 15 μm.

Commonly, fluidically-actuated soft robotic devices actuate from their inactive, flat state, to an actuated curved or deformed state, through the application of fluidic pressure. This is achieved, for example, by modulating the stiffness of each side of the device, through materials or thickness tuning. This induces a preferential deformation direction when the chamber is pressurized, thereby controlling the device's bending direction [29]. However, for a nerve cuff application, maintaining the wrapped state and ensuing consistent contact with the nerve would necessitate continuous pressurization, a scenario that is unsustainable in chronic application.

In order to eliminate the need for continuous pressure to maintain a curved state, we can consider reversing the approach to such actuation. Rather than actuating a device into a curved state, the device should be naturally curved, utilizing actuation to stiffen and straighten the device for implantation. In this way, the withdrawal of the pressure allows the device to return to its un-actuated, curved state. For nerve cuff applications, this aids in implantation, since the device is more rigid than most thin-film devices when actuated into its straight, stiffened state, and reduces the risk of nerve damage as only the relaxed, flexible device touches the nerve.

To achieve such a curved device starting with flat Parylene C, we turned to thermoforming. Thermoforming has recently been shown to be an effective strategy for achieving shaped neural implants based on Parylene C, including nerve cuff devices [38, 45–47]. Thermoforming involves heating the Parylene C above its glass transition temperature (60–90°C), inducing the relaxation and reordering of the polymer chains. When the heated Parylene C film is moulded into the desired shape, the polymer chains conform, and when cooled the chains are set in this new configuration. Using this approach, flat Parylene C films can be shaped into stable, 3D curled structures that are suitable for nerve cuff applications (Figure 2C i-iii). Annealing was performed at 100°C in our work as it minimizes thermal expansion in the Parylene C layers, helping to reduce stress imbalance in the Parylene C layers and subsequently, the stress transferred to the metal electronic layers [47]. Here, thermoforming was performed by wrapping the device around a 0.8 mm diameter carbon fiber rod and annealing in an oven. 0.8 mm was chosen as a close match to the intended demonstration application of a rodent sciatic nerve, though large or smaller diameters are easily achieved using different sizes. Pervious work does, however, suggest that a lower limit to this size is likely to lie around 100 μm diameter due to failures of the metal tracks [48].

After thermoforming our device into the desired cuff shape, fluidic actuation inflates the chamber causing the device to stiffen and straighten (Figure 2C iv–vi). While the dimensions of the cuff were set during the thermoforming process, the stability of this forming remains in question. This becomes of particular importance when considering the desire to be able to reinflate and reposition the device multiple times during surgery. In order to investigate the stability of the thermoformed structure, the inner diameter of the cuff was measured over 50 repeated pressurization/straightening, depressurization/relaxation cycles.

It can be seen in Figure 2D that, over the course of 50 straightening and bending cycles, there is a modest increase in the measured

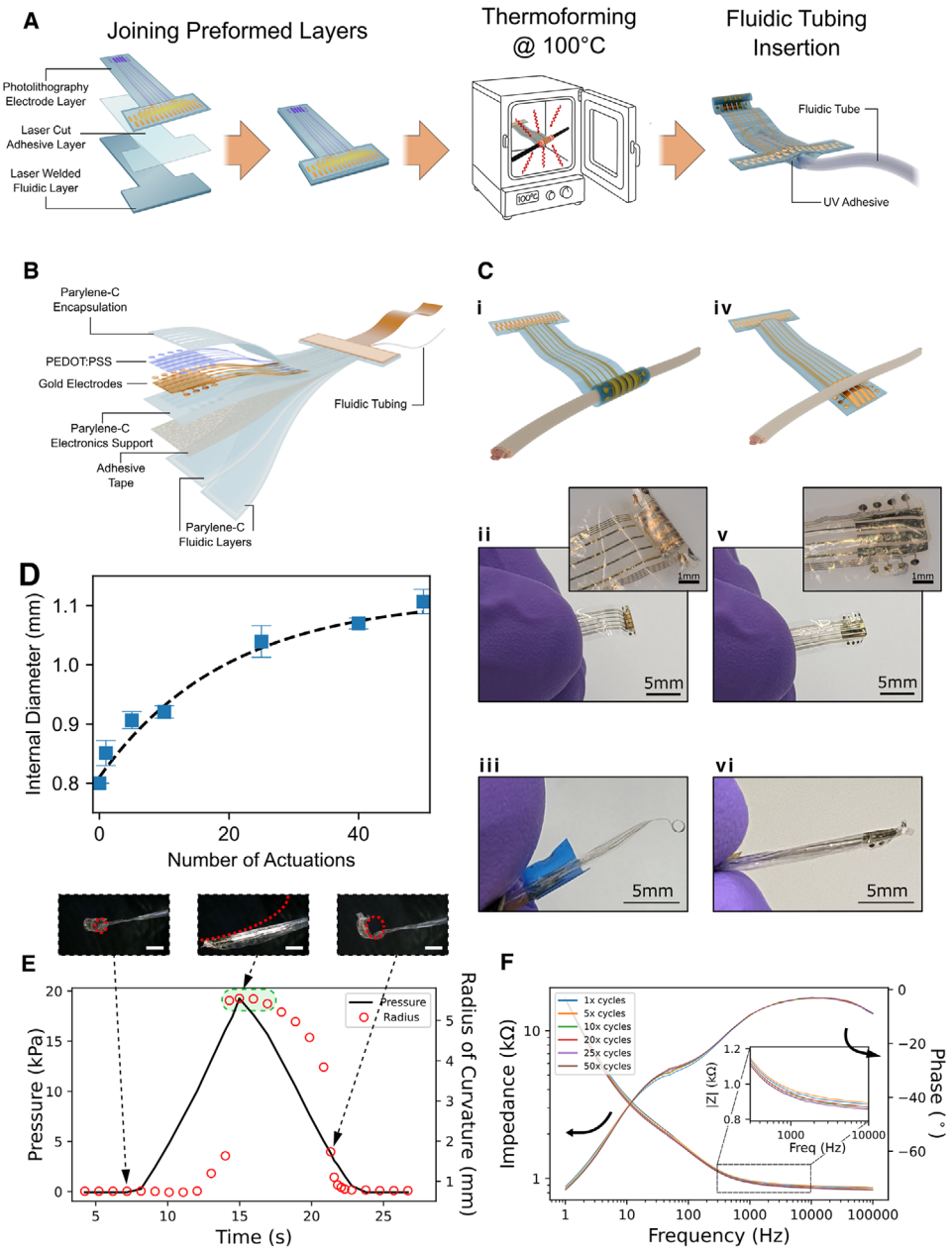

FIGURE 2 | Fabrication, thermoforming and electrical stability of actuated cuff electrodes. (A) Shaping steps of the nerve cuff, starting with combining the electrode and fluidic chamber layers, followed by thermoforming into the desired cuff radius, and finally introducing the fluidic tubed to integrate the device. (B) Overview of the cuff peripheral nerve implantable device structure. (C) Illustrations (i and iv) and images of the cuff style device in the rolled/deflated state (i–iii) and unrolled/inflated state (iv–vi). (D) Inner diameter of the thermoformed cuff device after repeated pneumatic actuation. Data are presented as average measured internal diameter ± standard deviation over 3 independently fabricated devices, along with least squares fitting to the data of a single-exponential approach-to-asymptote model. (E) Pressure-time and plot for a single actuation cycle along with the measured cuff radius at discrete time points. Above are images of the device at three pressures along with superimposed dashed red circles used to calculate the radius of curvature (scale bars are 2 mm). The four radii at the maximum pressure, highlighted in green, can be considered as "undefined" radii as there is no measurable curvature to the device at this point. (F) Electrochemical impedance spectroscopy, showing the impedance and phase response with frequency over multiple actuation cycles, demonstrating the electrical stability of the Au/PEDOT:PSS electrodes.

inner diameter of the thermoformed cuff, from the as-formed diameter of 0.8 mm to an expanded 1.1 mm after 50 cycles. Given the level of anatomical variation in nerve bundle diameter and the relatively high number of actuation cycles tested (normal use is expected to require only a few such cycles), we are confident that this level of change will have little effect on the efficacy of these devices.

In addition to resilience to repeated bending cycles, it is also important to understand the relationship between the applied fluidic pressure and device actuation during a single cycle. Figure 2E and Video S1 show the relationship between the applied pressure and the radius of curvature of the cuff, along with some example images used for the quantification of such. Interestingly, it is clear that there is a level of hysteresis between the pressure

and the actuation, with both the unrolling (increasing radius of curvature) and the rolling phases lagging behind the pressure. However, it can be seen that the device is fully rolled by the time the pressure returns to the starting level, indicating that the speed of actuation is dominated by the rate of pressure withdrawal. This allows precise control of the actuation during deployment such that a surgeon can very simply control the cuffing/uncuffing of the device while placing it to enable rapid repositioning.

In finally it is important to consider the electrical stability of the thin-film electrodes during such bending cycles. To evaluate the electrical stability of our devices we periodically performed electrochemical impedance spectroscopy (EIS) on the electrodes during the 50 cuffing-uncuffing cycles. The EIS reveals that, for the electrodes integrated into the nerve cuff devices, there is a negligible change in electrical performance over 50 repeated actuations of the device (Figure 2F).

2.3 | Rodent In Vivo Validation

To validate the feasibility of using the nerve cuff developed above, we looked at its use in interfacing with the sciatic nerve in a rodent model. The sciatic nerve was selected for its relatively large size, making it more comparable to human nerve bundles, thereby providing a physiologically relevant and practical model for demonstrating the concept of our ultra-thin soft-robotic implants.

For the implantation of the device, we approached the sciatic nerve with the device in its inflated, stiffened state from the underside of the nerve, ensuring the electrodes were placed in contact with the nerve (Figure 3Ai). The rigidity, enabled by the pressurization, allowed the device to be both placed in contact with the sciatic nerve and positioned without the use of additional handling tools during the surgical procedure. To stiffen and straighten the device, around 10 kPa of air pressure was applied manually to the cuff by the surgeon via a syringe during placement.

Once the cuff was correctly aligned beneath the sciatic nerve, ensuring that the base of the electrodes made contact, the device was manually deflated (Figure 3Aii). By removing the air pressure, the device transitioned from its actuated, rigid state back into a flexible, thin-film configuration. Thanks to the thermoforming step during manufacturing, the relaxed state of the device is curled, and it was seen that the device gently wrapped around the sciatic nerve bundle when returning to this state during depressurization (Figure 3B). Conformal contact with the nerve was achieved by the device due to capillary adhesion and conformal, thin-film design of the Parylene C substrate.

To validate the contact between the device and nerve from the thermoforming process, the sciatic nerve was externally stimulated to induce evoked compound motor action potentials (CMAPs). The resulting averaged CMAPs recorded on a single electrode are shown in Figure 3C, with the evoked CMAPs having a peak potential greater than the saturation level of the applier used (6.4 mV) after a 2.5 mA stimulation with the waveform recorded comparable with previously reported literature [49, 50]. Multiple CMAPs were able to be recorded across all 12 electrodes post-implantation (Figure 3D) and were consistent across all electrodes.

In the background of the baseline recordings taken from the sciatic nerve without any stimulation, an electrocardiogram (ECG) signal can be observed, representing the rat's heart rate at approximately 330 bpm, consistent with the heart rate of a rat under anesthesia [51] (Figure 3E). The presence of ECG signals in the baseline suggests that the cuff device maintains good conformal contact with the sciatic nerve following implantation. The characteristic ECG trace is visible not only in the raw data but also in the spectrogram of the raw trace. The ready appearance of this ECG signal is a clear indication of the good contact and low noise obtained in the recordings for this device. Indeed, this baseline ECG can even be seen in the spectrogram in the times between nerve stimulation events, Figure S3. While this presence of the ECG signal helps validate the quality of electrical contact achieved, it does also pose a challenge in terms of signal processing, wherein the ECG signal may be considered a unwanted artifact. However, given the relatively low power of this signal (around 20–30 dB below the power of the record CMAPs) and its periodicity, simple signal processing techniques can be applied to remove this article and leave a clearer picture of the sciatic activity.

3 | Discussion

In this work, we leveraged soft-robotic technologies to enable ultra-thin minimally-invasive neural interfaces. We explored the ability to create Parylene C based fluidic chambers through the optimization of laser power parameters and used the optimized Parylene C fluidic chamber design paradigm to create a proof-of-concept peripheral nerve implant to demonstrate the ability of thin-film fluidic soft-robotic technologies to safely deploy minimally-invasive neural interfaces within the body.

When using a CO_2 laser cutter to outline the design of a fluidic chamber made from a Parylene C bilayer, we observed the formation of heat-affected zones around the laser ablation site. This heat-affected zone caused the fusion of two 4 μm Parylene C layers, enabling the formation of a chamber able to support fluidic pressure. We have shown that, by optimizing the laser parameters, bonding during combined laser cutting and welding could be achieved between the two Parylene C layers. Through the combination of laser cutting and welding to bond the two layers, a resulting tensile bond strength of 24 MPa was achieved at the interface between these two layers. While lower than the tensile strength of pristine Parylene C, this bonding strength is higher than other reported tensile bonding strengths achieved when attempting to thermally bond two Parylene C coated wafers together, where bond strengths of 9.2 [52] and 3.2 MPa [53] were reported. The approach developed in this work produces welds with higher resulting tensile strength than previously reported whole-wafer bonding approaches, while also enabling spatially selective welding by restricting the thermal bonding to the laser-scribed area. After the formation of the fluidic chamber using the optimized laser settings, the ultra-thin bilayer Parylene C fluidic chamber was able to withstand

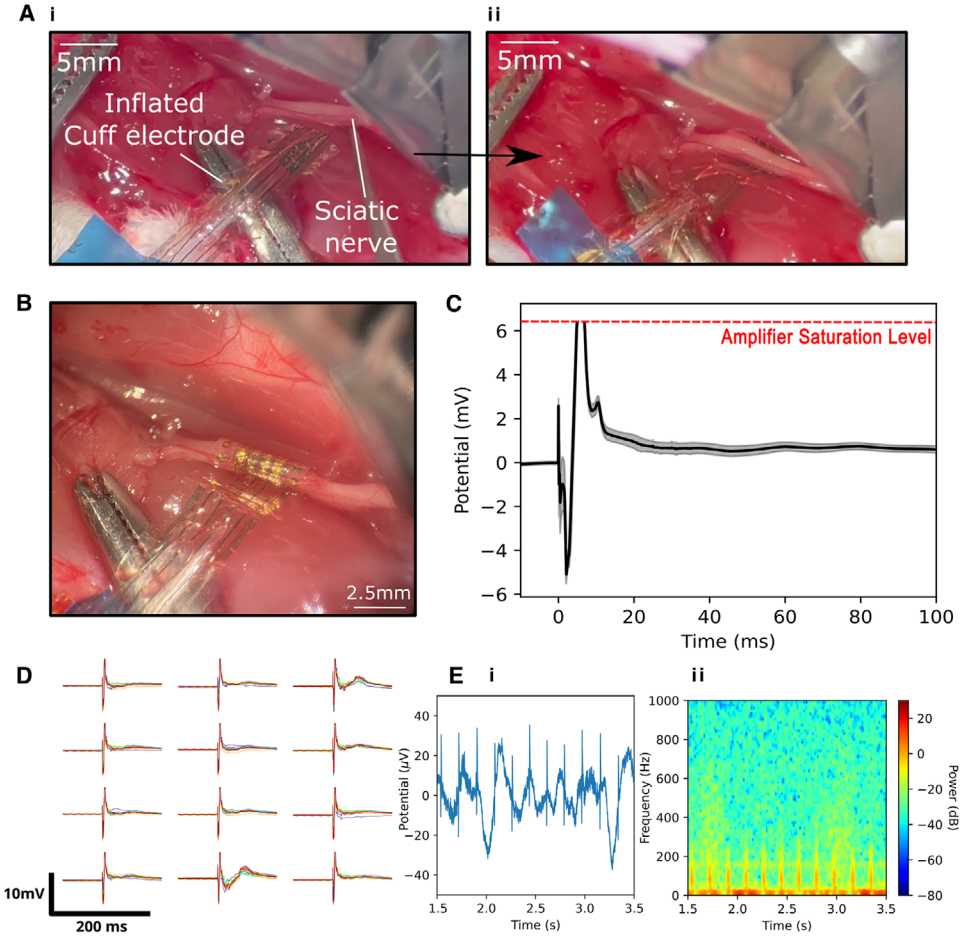

FIGURE 3 | In vivo testing of the cuff-style peripheral nerve implant. (A) Image series showing the implantation process of the cuff-style interface. (i) Inflated device placed underneath the sciatic nerve without the need for addition deployment tools around the nerve site. (ii) Withdrawal of pneumatic pressure to begin curling of the device. (B) Final cuffed state of the device around the sciatic nerve after implantation. (C) Representative averaged Compound Motor Action Potential (CMAP) recorded on a singular electrode after implantation in response to an external monophasic stimulation with the standard deviation in the data shaded in grey. Note the top of the CMAP here exceed the saturation level of the Intan Stimulation and Recoding system used, marked by the dashed red line. (D) A full recording map of the CMAPs obtained from all 12 electrodes on the nerve cuff device. (E) ECG signal recorded from the sciatic nerve in the i) baseline neural recordings and ii) observable in the resultant spectrogram.

an improved 78 kPa of pneumatic pressure, significantly outperforming previously reported silicone soft-robotic neural implants able to support maximal pneumatic pressures of just 12–35 kPa [21, 22, 29, 54].

In our investigation, we encountered a significant challenge with our CO_2 laser system when using it to create the Parylene C fluidic chamber, due to inconsistencies in the delivered laser power, exacerbated in more complex designs. This limitation hindered the efficacy of using the optimized laser parameters for complex curved design geometries, limiting the device shapes enabled in this initial investigation. Consequently, the adoption of a more advanced laser system that would ensure consistent power delivery for further work would allow the refinement of this approach in creating ultra-thin fluidic systems. Such a tool would facilitate the creation of more complex fluidic chamber designs, more in line with current PDMS-based fluidic devices where the shape can be more arbitrary. This would open up the design space when creating the fluidic chamber for integration into novel bioelectronic implants to enable more advanced shape actuation.

A cuff-type device successfully demonstrated the application of the ultra-thin fluidic chamber when integrated into a real-world neural interface device. Due to the ease of surgical handling, it facilitated straightforward placement and adjustment of the device through pneumatic actuation. Post-implantation, the nerve cuff was able to record induced CMAPs from the sciatic nerve, with the close contact of the nerve cuff to the sciatic nerve enabled by the ultra-thin design, allowing the visualization of ECG signals present within baseline nerve recordings. While the self-wrapping mechanism and performance around a nerve bundle of the thermoformed cuff-style device were similar to previously described thermoformed [38] and soft-robotic self-actuating nerve cuffs [20, 25, 26, 30], our approach enables the tool-free implantation of the cuff by using pneumatic pressure to straighten, rather than curl, the device during placement, and allows rapid tool-free readjustment of the device to optimize placement. This is not possible with previously reported shape-changing approaches, where the device permanently changes shape upon placement, whether through temperature increase to force shape-memory polymer-based actuation or fluid-based swelling of an attached actuation

layer. The approach is also preferable to recently reported electrochemical actuation mechanisms, which require exotic materials and a continuous electrical potential to maintain the cuffed shape, and achieve actuation over much longer time periods. The use of a Parylene C bilayer removes the need for the addition of novel materials to drive actuation, or any ongoing stimulus to maintain device contact, potentially facilitating faster translation when suitable clinical applications are identified.

The current design of the cuff-style device is, however, suitable only for interoperative applications due to the relatively low grip strength of the device. To address this limitation, the integration of helical designs within the cuff-style implant could allow the device to naturally anchor to the nerve, eliminating the need for sutures typically required to secure standard nerve cuff designs. This innovation could drastically reduce the invasiveness and complexity of the procedure, enhancing the device's applicability for longer-term monitoring and therapeutic interventions by providing a more stable and secure attachment to the nerve. Additionally, the primary challenge in adopting a purely minimally invasive approach for the implantation of these devices lies in the necessity to expose the sciatic nerve and the trauma this causes to the surrounding tissue. This procedure still requires a relatively invasive surgical intervention, necessary to allow wrapping a nerve interface cuff device around the nerve even with the self-wrapping designs proposed here. This introduces potential surgical complications during manual handling, especially as the size of the targeted nerve bundle size reduces

Initial validation was performed in an acute rodent model. Unfortunately, in this initial proof-of-concept work, we were unable to perform histology on the sciatic nerve post-implantation. However, as the cuff device naturally wraps around the nerve due to the thermoforming, we envision that the gentle wrapping of the cuff would prevent any crushing of the nerve. Indeed, benchtop measurements of the gripping strength of these devices showed the total force to be below the detection threshold of 1 mN, or below 30 Pa for this device geometry; significantly below the threshold for damage around 3 kPa [55]. If a final design is chosen for the application of the ultra-thin soft robotic chambers in an application for the peripheral nerve, full histology should be performed in the context of a chronic in vivo study to validate this assertion.

4 | Conclusions

In summary, we investigated how laser cutting and welding could be optimized to create hermetically sealed ultra-thin Parylene C fluidic chambers. By investigating the strength of the resulting bond when the two layers of Parylene C are processed using a CO_2 laser, we identified laser parameters that resulted in high bond strength for both full-layer cutting and localized welding of two layers of Parylene C. By using the combination of the two processing techniques, we were able to create a fully sealed pneumatic chamber suitable for integration with thin-film bioelectronics to enable actuation, with the resulting chamber being one of the thinnest implantable fluidic soft robotics actuators reported to date.

The resulting fluidic chamber had a higher maximal pressure tolerance than previously reported silicone-based approaches and, therefore is potentially suitable for integration into different types of bioelectronic implants to enable shape actuation, for example improving electrode contact in cochlea implants by dynamically adjusting curvature. Additionally, with further investigation into the welding-only effect explored initially in this work, one could envision the creation of microfluidic channels and chambers within a larger Parylene C device. In the future, we plan to explore the possibility of this effect being present in other thin-film polymer substrates, especially polyimide, providing alternative material options when designing next-generation shape-actuating devices, as well as further optimizing the welding of Parylene C, in particular increasing design complexity, leveraging a more consistent laser machine. To further develop the actuated nerve cuff demonstrated here, future works will look at the biocompatibility of the whole device, as well as exploring the long term stability of the electrodes with electrical stimulation and the histological impact of long term implantation of such structures to understand the feasibility of chronic use.

5 | Methods

5.1 | Tensile Testing

To create Parylene C test samples for tensile testing, 4 μm of Parylene C was deposited using a PDS 2010 Labcoter (Specialty Coating Systems) on a glass wafer coated with a 3% Micro 90 (VWR) soap solution. On top of the bottom 4 μm layer of Parylene C, 3% Micro 90 soap solution was spin-coated onto the Parylene C at 1500 rpm for 30 s to act as an anti-adhesive before a second layer of 4 μm layer of Parylene C was deposited. To create test samples, a VLS 2.30 CO_2 10.6 μm laser cutter (Universal Laser Systems) was used to create 5 mm lines in the two layers of Parylene C, with the power adjusted accordingly to cut or weld the Parylene C layers. A single-sided dumbbell shape was then cut out manually from the Parylene C using a scalpel, and the two layers of Parylene C were peeled apart manually to leave the processed edge in the center of the dumbbell sample. These samples were attached to a Tinius Olsen 1 ST tensile testing system with a 25 kN loadcell and pulled until sample failure, with the breaking force recorded.

5.2 | Fabrication of Fluidic Actuation Chambers

To form the Parylene C fluidic chambers, a glass slide was coated in a 3% Micro-90 soap solution before two subsequential 4 μm Parylene C depositions with a PDS Labcoter 2 (Specialty Coating Systems Ltd), with a 3% Micro-90 soap solution spin-coated at 1000 rpm onto the first layer of 4 μm Parylene C to act as an anti-adhesive. The outline of the required fluidic chamber design was laser cut using a CO_2 laser cutter (VLS2.30, Universal Laser Systems) at 4.5 W Power, 17.8 mm s^{-1} speed, and 1000 dpi. The welding of the outlined was performed at 0.24 W Power, 17.8 mm s^{-1} speed, and 1000 dpi with a 0.3 mm offset from the cut edge. After the fluidic chamber design was released from the glass slide, a PTFE tube (400 μm OD / 200 μm ID, Bohlender, VWR) was inserted into the neck of the design, and sealed with UV curing adhesive (Loctite 358, RS).

To complement the design of the thin Parylene C-based fluidic chamber, thin-film electronics were fabricated in an independent process on Parylene C. The design incorporated Au/PEDOT:PSS electrodes and interconnects, with the aim of producing electrodes that wouldn't interfere with the actuation and shape-change enabled by the fluidic chamber, and which are suitable for the thermoforming required to create the 3D wrapping devices.

5.3 | Fabrication and Characterization of Thin Film Electronics

To prepare the PEDOT:PSS, commercially available PEDOT:PSS solution (Heraeus Clevios PH1000) was mixed with 5% v/v Ethylene Glycol (Sigma–Aldrich), 0.05% wt. dodecyl benzene sulfonic acid (Sigma–Aldrich), and 1% 3-Glycidyloxypropyl trimethoxysilane (Sigma–Aldrich). After preparing the PEDOT:PSS solution, 2% w/w of D-Sorbitol (Sigma–Aldrich) was added. This solution was sonicated for 20 min to ensure homogenous mixing. The solution was then filtered using a PTFE 0.45 μm membrane filter before use.

To begin the fabrication process, a 100 mm Silicon wafer (Test Grade, Pi-Kem) was coated with 2 μm Parylene C using a PDS Labcoter 2 (Specialty Coating Systems Ltd). For the metal interconnects and electrode pads, AZnlof 2035 (Microchemicals GmbH) photoresist was spin-coated onto the bottom Parylene C substrate at an initial 500 rpm for 5 s, followed by a 3000 rpm (6000 rpm s^{-1}) for 30 s, to achieve a resist thickness of 3–3.5 μm. After spin coating, a soft bake for 60 s at 100°C was applied to the resist.

To produce the interconnect and electrode layout, the wafer was exposed to ultraviolet (UV) light (8 s, 80 mJ cm^2) using an MA/BA6 contact mask aligner (Karl Suss) through a plastic photomask (JD Photodata). A hard baking step was applied for 60 s at 115°C before developing in AZ726 (MicroChemicals GmbH) for 120 s. After developing, the samples were rinsed using deionized (DI) water to remove excess developer and dried using compressed nitrogen. The Parylene C substrate with developed resist was cleaned and activated with O_2 plasma (Diener Pico) at 0.6 mbar for 60 s at 100 W. 10 nm of Ti and 100 nm of Au were deposited sequentially on the activated substrate under vacuum ($<6 \times 10^{-7}$ mTorr) in a PVD75 E-Beam system (Kurt Lesker), with a 10 min rest period between each deposition.

The substrates were soaked in acetone for 1 h to perform lift-off with gentle agitation on a shaker plate at 100 rpm, before spraying with acetone and gently wiping with a sponge to remove any remaining excess resist. The substrates were washed with isopropyl alcohol before inspection to ensure complete lift-off under a microscope.

After metal deposition and the AZnlof 2035 was full removal, the entire substrate was activated with O_2 plasma (Diener Pico) at 0.6 mbar for 60 s at 100 W. The prepared PEDOT:PSS solution was spin-coated twice at 1500 rpm for 30 s with a 60 s soft-bake at 110°C between spin-coatings to achieve an approximate thickness of 200 nm, reenforcing the mechanical and electrical stability of the metal tracks, and increasing longevity following the work of Oldroyd et al. [56]. The substrate was then baked for 1 h at 120°C to fully cross-link the PEDOT:PSS. After baking, the devices were soaked in DI water for 3×15 min in order to wash out excess PSS from the PEDOT:PSS film.

To pattern the interconnect and electrode layout onto the PEDOT:PSS film, AZ5214E image reversal photoresist (Microchemicals GMBH) was spin-coated at 500 rpm for 5 s and 2500 rpm for 30 s to achieve a film thickness of 2–2.5 μm. After a soft bake at 110°C for 120 s, the substrate was exposed to UV light (20 s, 80 mJ cm^2) through a plastic photomask (JDPhotodata) and then developed in AZ726 developer for 30 s. The PEDOT:PSS was etched using Reactive Ion Etching (Oxford Plasma Pro 80 RIE, 160 W, 50 sccm O_2, 5 sccm CF_4).

A second 2 μm layer of Parylene C was deposited on the substrate to act as the insulation layer of the electronic component, before AZ 10xt (Merck) photoresist was spin-coated at an initial 500 rpm for 5 s, followed by a 3000 rpm (6000 rpm s^{-1}) for 30 s, to achieve a resist thickness of 6 μm. After a soft bake at 110°C for 120 s, the substrate was exposed to UV light (20 s, 80 mJ cm^2) and then developed in 1:4 AZ400k:DI water solution for 4 min. The outline of the device was then etched using Reactive Ion Etching (RIE) (Oxford Plasma Pro 80 RIE, 160 W, 50 sccm O_2, 5 sccm CF_4) before the remaining resist was washed off with acetone. A 3% soap solution (Micro 90, VWR) was spin-coated onto the wafers at 1000 rpm for 30 s before a 2 μm sacrificial layer of Parylene C was deposited.

To open the electrode and interconnection pads, AZ 10xt (Merck) photoresist was spin-coated at an initial 500 rpm for 5 s, followed by a 3000 rpm (6000 rpm s^{-1}) for 30 s, to achieve a resist thickness of 6 μm. After a soft bake at 110°C for 120 s, the substrate was exposed to UV light (20 s, 80 mJ cm^2) and then developed in 1:4 AZ400k:DI water solution for 4 min. The electrodes were exposed with Reactive Ion Etching (Oxford Plasma Pro 80 RIE, 160 W, 50 sccm O_2, 5 sccm CF_4) to remove the 4 μm of Parylene C from the sacrificial and insulation layers.

After exposing the electrode surface with RIE, the prepared PEDOT:PSS solution was spin-coated once at 1500 rpm for 30 s and twice at 3000 rpm for 30 s with a 60 s soft-bake at 110°C between spin-coatings to achieve an approximate thickness of 150 nm. Between spin-coatings, DI-water was used to carefully remove PEDOT:PSS on the exposed interconnection pads to prevent shorting after connection. After spin-coating, the sacrificial layer of Parylene C was peeled off to remove the excess spin-coated PEDOT:PSS, leaving the layer of PEDOT:PSS solely on the electrode pads. The substrate was then baked for 1 h at 120°C to fully cross-link the PEDOT:PSS. After baking, the devices were soaked in DI water for 3×15 min in order to wash out excess PSS from the PEDOT:PSS film.

When the devices were finished, a small amount of DI-water was used to help release each device from the silicon wafer and transferred to a glass slide. The electronics were bonded to an FFC cable (RS) using a Finetech bonder (Pico Ma) and anisotropic film (ACF) tape. The electrode array was finally bonded to the Parylene C fluidic chamber to form the full device using 5 μm double-sided adhesive (Nikko).

Electrochemical Impedance Spectroscopy (EIS) was performed on each electrode using a Palmsens4 potentiostat. Electrodes were characterized in a phosphate buffered saline solution (0.01 M, Sigma–Aldrich), with a platinum (Goodfellow) counter electrode, and Ag/AgCl reference electrode (Ossila).

5.4 | Pressure Testing

Fluidic chambers fabricated specifically for pressure testing were created follow the same process as for the nerve cuff devices above. These measured 5 × 10 mm, with a 5 × 5 mm neck for tubing insertion. The tubing was secured in place using the same UV curing adhesive. To measure the fluidic pressure while testing, the Parylene C fluidic chambers were connected to a syringe via a 3D-printed t-connector that was connected to an MXP5100GP pressure sensor (NXP), with the pressure data recorded via an Arduino Mega. To characterize the maximum pressure of the devices, a 10 ml syringe pump (KD Scientific) was connected to the system and the devices were inflated using either air or DI water at 1 mL min^{-1}. The measurements were stopped after sudden loss of pressure indicating catastrophic failure of the fluidic chamber.

For assessment of the device actuation with pressure (Figure 2E), fully formed neve cuff devices, including the electronics layer, we attached to the same pressure sensor and inflated with the same syringe pump. Here 2 ml of air was injected at 8 mL min^{-1}, reaching a pressure significantly below the maximums reported, but still sufficient to fully straighten the device. Simultaneously, video of the device being inflated was recorded using a Keyence VHX S600 digital microscope. From this video, the radius of curvature was assessed using imageJ software.

For this measurement the device was inflated with air at 8 mL min^{-1} to a total volume of 2 mL. While this inflates the device to a pressure significantly below its maximum, it was still sufficient to fully straighten the device.

5.5 | Thermoforming

After the fabrication of the soft-robotic fluidic actuator and the thin-film electronics, and joining the two components, the thermoforming was performed on the combined device. For this, devices were wrapped around a 0.8 mm diameter Carbon Fiber rod (Easy Composites Ltd) and affixed into the cuff shape temporarily using 50 μm Kapton tape (RS). The devices were then annealed at 100°C for 12 h inside an oven (FiStream).

5.6 | Rodent In Vivo Testing

All animal procedures were carried out in accordance with the UK Animals (Scientific Procedures) Act, 1986. Work was approved by the Animal Welfare and Ethical Review Body of the University of Cambridge, and was approved by the UK Home Office (project license number PP5478947).

A Sprague Dawley female rat ~150–200 g in weight (Charles River, UK) was anesthetized with isoflurane (2.25% v/v in medical oxygen). Body temperature was monitored and maintained using a thermal blanket. The sciatic nerve was accessed at the level of the femur and an actuated device was implanted. A steel plate was implanted under the nearby skin and used as an electrical ground. The device and ground were connected to an electrophysiology acquisition system (Intan RHS stim/recording system, Intan Technologies). Anesthesia levels were then lowered to 1.25% to perform electrophysiology recording and stimulation experiments. To provide stimulation to the sciatic nerve, a platinum hook was placed around the sciatic nerve, and connected to the Intan RHS system through an RHS headstage. To generate compound motor action potentials (CMAPs), monophasic anodic current pulses were applied through the platinum hook at 2.5 mA for 33.33 μs to induce contraction within the leg. The resulting CMAPs were recorded from the implanted peripheral nerve devices connected to the Intan RHS system through an RHS headstage. After recording the CMAPs, the resulting traces were processed in MATLAB using a 50 Hz Notch Filter and a 250 Hz Butterworth Low Pass Filter.

5.7 | Statistical Analysis

All data all figures presented in this work with an uncertainty represent mean ± standard deviation over 3 independently fabricated devices or samples.

Author Contributions

The project was initially conceived and initiated by L.C. and C.M.P. Device fabrication, development and testing were carried out by L.C. and J.G.T. In vitro experiments were designed and analyzed by L.C. Rodent experiments were carried out by L.C. and A.C.L. L.C. performed and analyzed the electrical stimulation experiments and data. J.G.T. provided the drawing renders of the device. L.C. produced the first draft of the manuscript, C.M.P., J.G.T., and L.C. edited the manuscript, and J.G.T. produced the final draft of the manuscript. C.M.P. and G.G.M. oversaw the project.

Acknowledgements

L.C. acknowledges funding from the U.K. Engineering and Physical Sciences Research Council Centre for Doctoral Training in Sensor Technologies for a Healthy and Sustainable Future (EP/S023046/1). A.C.L. acknowledges funding from the University of Cambridge Borysiewicz Fellowship program. J.G.T is supported by the National Institute for Health Research Invention for Innovation award (NIHR203355). C.M.P. acknowledges funding from the University of Cambridge Borysiewicz Fellowship program, U.K. Engineering and Physical Sciences Research Council IAA award, and the Biotechnology and Biological Sciences Research Council David Phillips Fellowship. The devices were built in the laboratory for prototyping soft neuroprosthetic technologies, funded by the Sir Jules Thorn charitable trust (233838).

Conflicts of Interest

C.M.P. and G.G.M are inventors on a patent related to this work filed by Cambridge Enterprise Ltd. (No. PCT/GB2020/051684, filed 13 July 2020). The authors declare that they have no other competing interests.

Data Availability Statement

The data that support the findings of this study are available from the corresponding author upon reasonable request.

References

1. R. M. Dorrian, A. V. Leonard, and A. Lauto, "Millimetric Devices for Nerve Stimulation: A Promising Path Towards Miniaturization," *Neural Regeneration Research* 19 (2024): 1702–1706.

2. J. P. O'Reardon, P. Cristancho, and A. D. Peshek, "Vagus Nerve Stimulation (VNS) and Treatment of Depression: To the Brainstem and Beyond," *Psychiatry (Edgmont)* 3 (2006): 54–63.

3. S. E. Krahl, "Vagus Nerve Stimulation for Epilepsy: A Review of the Peripheral Mechanisms," *Surgical Neurology International* 3 (2012): S47–S52.

4. A. K. Das, M. D. White, and P. A. Longhurst, "Sacral Nerve Stimulation for the Management of Voiding Dysfunction," *Reviews in Urology* 2 (2000): 43–60.

5. T. Meissnitzer, S. Trubel, R. Posch-Zimmermann, and M. W. Meissnitzer, "CT-Guided Lead Placement for Selective Sacral Neuromodulation to Treat Lower Urinary Tract Dysfunctions," *American Journal of Roentgenology* 205 (2015): 1139–1142.

6. X. Wang and J. D. Chen, "Therapeutic Potential and Mechanisms of Sacral Nerve Stimulation for Gastrointestinal Diseases," *Journal of Translational Internal Medicine* 11 (2023): 115–127.

7. M. Ortiz-Catalan, R. Brånemark, B. Håkansson, and J. Delbeke, "On the Viability of Implantable Electrodes for the Natural Control of Artificial Limbs: Review and Discussion," *BioMedical Engineering OnLine* 11 (2012): 33.

8. K. A. Yildiz, A. Y. Shin, and K. R. Kaufman, "Interfaces with the Peripheral Nervous System for the Control of a Neuroprosthetic Limb: A Review," *Journal of NeuroEngineering and Rehabilitation* 17 (2020): 43.

9. H. Kim, A. M. Dingle, J. P. Ness, et al., "Cuff and Sieve Electrode (CASE): The Combination of Neural Electrodes for Bi-Directional Peripheral Nerve Interfacing," *Journal of Neuroscience Methods* 336 (2020): 108602.

10. T. Boretius, J. Badia, A. Pascual-Font, et al., "A Transverse Intrafascicular Multichannel Electrode (TIME) to Interface with the Peripheral Nerve," *Biosensors and Bioelectronics* 26 (2010): 62–69.

11. A. Carnicer-Lombarte, D. G. Barone, I. B. Dimov, et al., "Mechanical Matching of Implant to Host Minimises Foreign Body Reaction," *bioRxiv* (2019): 829648.

12. C. Russell, A. D. Roche, and S. Chakrabarty, "Peripheral Nerve Bionic Interface: A Review of Electrodes," *International Journal of Intelligent Robotics and Applications* 3 (2019): 11–18.

13. D. G. Kline and L. T. Happel, "A Quarter Century's Experience with Intraoperative Nerve Action Potential Recording," *Canadian Journal of Neurological Sciences* 20 (1993): 3–10.

14. K. S. Rice and S. A. Skinner, "Koht, Sloan, Toleikis's Monitoring the Nervous System for Anesthesiologists and Other Health Care Professionals," *Intraoperative Electromyography* (Eds: C. N. Seubert, J. R. Balzer), (Springer International Publishing 2023): 91–144.

15. N. A. Zelenski, T. Oishi, and A. Y. Shin, "Intraoperative Neuromonitoring for Peripheral Nerve Surgery," *Journal of Hand Surgery* 48 (2023): 396–401.

16. R. Goldbrunner, M. Weller, J. Regis, et al., "EANO Guideline on the Diagnosis and Treatment of Vestibular Schwannoma," *Neuro Oncology* 22 (2020): 31–45.

17. M. Yu, C. Wang, H. Cui, et al., "Self-Closing Stretchable Cuff Electrodes for Peripheral Nerve Stimulation and Electromyographic Signal Recording," *ACS Applied Materials & Interfaces* 15 (2023): 7663–7672.

18. A. Carnicer-Lombarte, S.-T. Chen, G. G. Malliaras, and D. G. Barone, "Foreign Body Reaction to Implanted Biomaterials and Its Impact in Nerve Neuroprosthetics," *Frontiers in Bioengineering and Biotechnology* 9 (2021): 622524.

19. E. B. Dolan, C. E. Varela, K. Mendez, et al., "An Actuatable Soft Reservoir Modulates Host Foreign Body Response," *Science Robotics* 4 (2019): 7043.

20. Y. Zhang, N. Zheng, Y. Cao, et al., "Climbing-Inspired Twining Electrodes using Shape Memory for Peripheral Nerve Stimulation and Recording," *Science Advances* 5 (2019): aaw1066.

21. B. J. Woodington, V. F. Curto, Y.-L. Yu, et al., "Electronics with Shape Actuation for Minimally Invasive Spinal Cord Stimulation," *Science Advances* 7 (2021): abg7833.

22. S. Song, F. Fallegger, A. Trouillet, K. Kim, and S. P. Lacour, "Deployment of An Electrocorticography System with a Soft Robotic Actuator," *Science Robotics* 8 (2023): add1002.

23. C. Dong, A. Carnicer-Lombarte, F. Bonafè, et al., "Electrochemically Actuated Microelectrodes for Minimally Invasive Peripheral Nerve Interfaces," *Nature Materials* 23 (2024): 969–976.

24. H. Zheng, Z. Zhang, S. Jiang, et al., "A Shape-Memory and Spiral Light-Emitting Device for Precise Multisite Stimulation of Nerve Bundles," *Nature Communications* 10 (2019): 2790.

25. D. Terutsuki, H. Yoroizuka, S. Osawa, et al., "Totally Organic Hydrogel-Based Self-Closing Cuff Electrode for Vagus Nerve Stimulation," *Advanced Healthcare Materials* 11 (2022): 2201627.

26. L. Hiendlmeier, F. Zurita, and J. Vogel, "4D-Printed Soft and Stretchable Self-Folding Cuff Electrodes for Small-Nerve Interfacing," *Advanced Materials* 35 (2023): 2210206.

27. C. Dong and G. G. Malliaras, "Recent Advances in Stimuli-Responsive Materials and Soft Robotic Actuators for Bioelectronic Medicine," *Advanced Materials* 37 (2025): 2417325.

28. S. Rezaei, Y. Xu, and S. W. Pang, "Control of Neural Probe Shank Flexibility by Fluidic Pressure in Embedded Microchannel using PDMS/PI Hybrid Substrate," *PLoS One* 14 (2019): 0220258.

29. H. Moon, B. Park, N. Chou, K.-S. Park, S. Lee, and S. Kim, "Soft-Actuated Cuff Electrodes with Minimal Contact for Bidirectional Peripheral Interfaces," *Advanced Materials* 37 (2025): 2409942.

30. M. A. González-González, A. Kanneganti, A. Joshi-Imre, et al., "Thin Film Multi-Electrode Softening Cuffs for Selective Neuromodulation," *Scientific Reports* 8 (2018): 16390.

31. Z. Zhu, Z. Yan, S. Ni, et al., "Tissue/Organ Adaptable Bioelectronic Silk-Based Implants," *Advanced Materials* 36 (2024): 2405892.

32. T. Goto, K. Sakai, Y. Mizuno, M. Yamaguchi, and T. F. Teshima, "Self-Folding Graphene Cuff Electrodes for Peripheral Nerve Stimulation," *APL Materials* 13 (2025): 031107.

33. J. G. Troughton and C. M. Proctor, "Laser Micromachining for Bioelectronics: Past, Present, and Future," *Small Methods* (2025): 01560.

34. N. Farokhnia, A. Caprio, V. Kashyap, et al., "A Catheter-Deployable Soft Robotic Inflatable Basket for Enhanced Conformability to the Left Atrium of the Heart," *Advanced Healthcare Materials* 9 (2020): 1900951.

35. A. M. Cobo, C. E. Larson, K. Scholten, et al., "Parylene-Based Cuff Electrode With Integrated Microfluidics for Peripheral Nerve Recording, Stimulation, and Drug Delivery," *Journal of Microelectromechanical Systems* 28 (2019): 36–49.

36. A. Carnicer-Lombarte, A. J. Boys, A. Güemes, et al., "Ultraconformable Cuff Implants for Long-Term Bidirectional Interfacing of Peripheral Nerves at Sub-Nerve Resolutions," *Nature Communications* 15 (2024): 7523.

37. J. Ortigoza-Diaz, K. Scholten, C. Larson, et al., "Techniques and Considerations in the Microfabrication of Parylene C Microelectromechanical Systems," *Micromachines (Basel)* 9 (2018): 422.

38. F. Zurita, S. Freko, L. Hiendlmeier, et al., "Thermoformed Parylene-C Cuff Electrodes for Small Nerve Interfacing," *Advanced NanoBiomed Research* 4 (2024): 2300102.

39. J. G. Troughton, P. Brige, M. Ramuz, and I. Flexible, "Pulse Oximetry Sensors: Toward Long-Term Monitoring of Blood Oxygen Saturations," *Biomedical Materials & Devices* 1 (2023): 912–924.

40. R. B. Rashid, R. J. Ciechowski, and J. Rivnay, "Self-Aligned, Laser-Cut Organic Electrochemical Transistors," *Flexible and Printed Electronics* 5 (2020): 014007.

41. M. Mueller, C. Boehler, J. Jaeger, M. Asplund, and T. Stieglitz, "A Double-Sided Fabrication Process for Intrafascicular Parylene C Based Electrode Arrays," in *2016 38th Annual International Conference of the IEEE Engineering in Medicine and Biology Society (EMBC)* (2016), 2798–2801.

42. M. Mueller, N. de la Oliva, J. del Valle, I. Delgado-Martínez, X. Navarro, and T. Stieglitz, "Rapid Prototyping of Flexible Intrafascicular Electrode Arrays by Picosecond Laser Structuring," *Journal of Neural Engineering* 14 (2017): 066016.

43. F. Kohler, M. Schuettler, and T. Stieglitz, "Parylene-Coated Metal Tracks for Neural Electrode Arrays - Fabrication Approaches and Improvements Utilizing Different Laser Systems," in *2012 Annual International Conference of the IEEE Engineering in Medicine and Biology Society* (2012), 5133.

44. C. Henle, C. Hassler, F. Kohler, M. Schuettler, and T. Stieglitz, "Mechanical Characterization of Neural Electrodes based on PDMS-Parylene C-PDMS Sandwiched System," in *2011 Annual International Conference of the IEEE Engineering in Medicine and Biology Society* (2011), 640–643.

45. B. J. Kim, B. Chen, M. Gupta, and E. Meng, "Formation of Three-Dimensional Parylene C Structures via Thermoforming," *Journal of Micromechanics and Microengineering* 24 (2014): 065003.

46. B. J. Kim, B. Chen, M. Gupta, and E. Meng, "Three Dimensional Transformation of Parylene Thin Film Structures via Thermoforming," in *2013 IEEE 26th International Conference on Micro Electro Mechanical Systems (MEMS)* (2013), 339–342.

47. B. Thielen and E. Meng, "Characterization of Thin Film Parylene C Device Curvature and the Formation of Helices via Thermoforming," *Journal of Micromechanics and Microengineering* 33 (2023): 095007.

48. C. D. Lee and E. Meng, "Mechanical Properties of Thin-Film Parylene–Metal–Parylene Devices," *Frontiers in Mechanical Engineering* 1 (2015): 00010.

49. M. N. Hamad, N. Boroda, D. B. Echenique, et al., "Compound Motor Action Potentials During a Modest Nerve Crush," *Frontiers in Cellular Neuroscience* 16 (2022): 798203.

50. S. Lee, S. Sheshadri, Z. Xiang, et al., "Selective Stimulation and Neural Recording on Peripheral Nerves using Flexible Split Ring Electrodes," *Sensors and Actuators, B: Chemical* 242 (2017): 1165–1170.

51. A. Tsukamoto, K. Serizawa, R. Sato, J. Yamazaki, and T. Inomata, "Vital Signs Monitoring During Injectable and Inhalant Anesthesia in Mice," *Experimental Animals* 64 (2015): 57–64.

52. H. Noh, K. Moon, A. Cannon, P. J. Hesketh, and C. P. Wong, "Wafer Bonding using Microwave Heating of Parylene Intermediate Layers," *Journal of Micromechanics and Microengineering* 14 (2004): 625–631.

53. H. Kim and K. Najafi, "Characterization of Low-Temperature Wafer Bonding Using Thin-Film Parylene," *Journal of Microelectromechanical Systems* 14 (2005): 1347–1355.

54. L. Coles, D. Ventrella, A. Carnicer-Lombarte, et al., "Origami-Inspired Soft Fluidic Actuation for Minimally Invasive Large-Area Electrocorticography," *Nature Communications* 15 (2024): 6290.

55. B. Rydevik, G. Lundborg, and U. Bagge, "Effects of Graded Compression on Intraneural Blood Flow: An In Vivo Study on Rabbit Tibial Nerve," *Journal of Hand Surgery* 6 (1981): 3–12.

56. P. Oldroyd, J. Gurke, and G. G. Malliaras, "Stability of Thin Film Neuromodulation Electrodes under Accelerated Aging Conditions," *Advanced Functional Materials* 33 (2023): 2208881.

Supporting Information

Additional supporting information can be found online in the Supporting Information section.

Supporting file: admt70677-sup-0001-SuppMat.docx

Supporting file: admt70677-sup-0002-VideoS1.mp4